Biobased Epoxidized Castor Oil Covalent Adaptable Networks Adhesives Reinforced with Recycled Carbon Fibers

Macromolecular Rapid Communications

Macromolecular Rapid Communications
www.mrc-journal.de

RESEARCH ARTICLE OPEN ACCESS

Biobased Epoxidized Castor Oil Covalent Adaptable Networks Adhesives Reinforced with Recycled Carbon Fibers

Alberto Cellai[1] | Rafael Turra Alarcon[2] | Bernhard Sölle[3] | Elisabeth Rossegger[3] | Valentina Casalegno[1] | Milena Salvo[1] | Marco Sangermano[1]

[1]Politecnico di Torino, Dipartimento di Scienza Applicata e Tecnologia, Torino, Italy | [2]Universidade de São Paulo-USP, Instituto de Química de São Carlos, São Carlos, SP, Brazil | [3]Polymer Competence Center Leoben GmbH (PCCL), Leoben, Austria

Correspondence: Marco Sangermano (marco.sangermano@polito.it)

Received: 26 September 2025 | **Revised:** 6 November 2025 | **Accepted:** 7 November 2025

Keywords: adhesive | biobased | covalent adabtable networks | rebonding | transesterification | vitrimer composite | vitrimer

ABSTRACT

The development of sustainable, smart, and functional adhesives is crucial in advancing environmentally friendly materials. In this study, a fully biobased adhesive based on Covalent Adaptable Networks (CANs) is presented, integrating epoxidized castor oil (ECO) as the bio-based monomer and a novel eugenol-based phosphate ester (EUGP) as the transesterification catalyst. The system was further enhanced with Recycled Carbon Fibers (RCF) as reinforcing filler. The curing process was thermally initiated using Ytterbium(III) trifluoromethanesulfonate (YTT), enabling efficient crosslinking even at room temperature over 24 h, permitting an eco-friendly production. Extensive characterizations were conducted. FT-IR confirmed high conversion rates, even with 20 phr of RCF, proving the curing efficiency. DSC revealed curing kinetics, and DMTA revealed a tunable glass transition temperature (0–10 °°C) depending on the filler content. Rheological stress-relaxation tests demonstrated rapid stress relaxation (1000 s at 70 °°C), confirming dynamic bond exchange and reprocessability. Contact angle analysis confirmed the presence of hydrophobic surfaces, which enhance moisture resistance. TGA indicated thermal stability up to 105 °°C. Mechanical tests performed on different joined substrates (metals and ceramic composites) showed that both adhesive bulk and joint strength at room temperature increased with fiber loading. Rebonded joints retained 74–91% of their initial strength after two repair cycles. By exploiting transesterification chemistry, bio-based materials, and recycled conductive fillers, this study highlights a sustainable alternative to conventional adhesives. The results indicate that the analyzed fully biobased adhesive offers promising applications in flexible electronics, smart adhesives, and advanced composites, supporting the transition toward more environmentally responsible materials.

1 | Introduction

Thermosetting polymers are widely used in developing adhesive formulations due to their excellent mechanical properties, thermal stability, and chemical resistance. However, their permanent crosslinked structure prevents reshaping, repairing, and recycling, leading to significant environmental concerns. Unlike thermoplastics, which can be remelted and reformed, thermosets degrade upon heating, making conventional recycling methods inefficient. To address this challenge, researchers have explored Covalent Adaptable Networks (CANs), as a class of polymers with dynamic covalent bonds that allow network rearrangement under external stimuli, such as heat or chemical triggers, with particular attention from our group and from many other groups

to design bio-based systems together with dynamic covalent network properties [1–15] through comprehensive mechanistic and materials perspectives.

The concept of CANs was first explored by Tobolsky in 1956, by investigating the stress-relaxation behavior of polyester urethane elastomers via associative bond-exchange reactions [16], but the field was truly pioneered by Leibler et al. in 2011, who introduced transesterification as a key mechanism for network rearrangement [17]. This discovery allowed crosslinked materials to undergo topological rearrangements upon heating without losing their mechanical integrity, making them recyclable and reprocessable, and it opened the door to a wide family of associative and dissociative CANs with tunable rheology, creep resistance, and reprocessability [2, 3, 16, 18–39].

CANs are broadly categorized based on their bond-exchange mechanisms into two main types: dissociative and associative networks. Dissociative CANs rely on bond cleavage and reformation, temporarily reducing the crosslink density, leading to a transition from a solid to a liquid-like state, often at the expense of mechanical integrity over repeated cycles. Associative CANs, in contrast, maintain a constant crosslink density through bond-exchange reactions, ensuring material stability during reprocessing, an aspect largely leveraged in epoxy vitrimers developed by Sangermano and co-workers [1, 15, 19, 20, 40, 41] and deeply rationalized in several mechanistic and theoretical contributions from other groups [24–27]. Among associative mechanisms, transesterification has gained particular attention for its efficiency and suitability in bio-based systems, although other exchange reactions, including dioxaborolane metathesis, imine (polyimine) exchange, dynamic alkoxyamine, siloxane, disulfide, and urethane/oxa-Michael chemistries, have been powerfully exploited to tailor creep, viscosity, topology freezing temperature, and recyclability [27–29, 33–37, 42].

Transesterification involves the exchange of ester groups between polymer chains, facilitating controlled network rearrangement without depolymerization. This mechanism is highly desirable for next-generation crosslinked adhesives, as it allows self-healing, rebonding and improved longevity in the circular stream thanks to reprocessability. The introduction of catalysts further enhances the exchange reaction rate and efficiency, making transesterification faster and a key strategy for CANs development.

Within this frame we have designed reprocessable biobased adhesives starting from epoxidized castor oil as precursor. Because of the low thermomechanical properties of the crosslinked polymeric matrix, the formulations were reinforced by dispersing recycled carbon fibers (RCF) with the aim to enhance the mechanical performance of the biobased adhesives. The castor oil was selected based on previous studies, which showed its good dynamic covalent bond properties because of the simultaneous presence of hydroxyl and ester groups in the crosslinked matrix. The dynamic covalent bond activation can be achieved in the presence of suitable transesterification catalysts.

Yet, traditional catalysts are often petroleum-derived and raise sustainability concerns. To overcome this limitation, a fully bio-based transesterification catalyst synthesized from eugenol (EUGP), enabling a greener approach to dynamic covalent bonding when combined with epoxidized castor oil as the bio-based monomer [43].

The curing process of the biobased adhesive formulations was investigated by DSC and FTIR analysis, showing the effect of the presence of the RCF on curing behavior. The crosslinked adhesive was fully characterized by DMTA and mechanical analysis. Dynamic bond-exchange efficiency was evaluated by a stress-relaxation test. Additionally, recyclability and rebonding assessments were performed to evaluate its feasibility as a sustainable alternative to conventional adhesives, in line with the broader methodological framework proposed in recent reviews and mechanistic works on CANs [27, 35, 36, 38, 39].

2 | Materials and Methods

2.1 | Materials

Epoxidized castor oil (ECO) was achieved by epoxidizing castor oil. The chemical structure of ECO is visible in Figure 1a [44].

Castor oil (CO) was purchased from Mundo dos Óleos (Brasília, Brazil). The catalyst Amberlite IR-120, glacial acetic acid (≥99), hydrogen peroxide (50%, H_2O_2), magnesium sulfate (≥99.5%), ethyl acetate, and deuterated chloroform ($CDCl_3$, 99.8% D) were acquired from Sigma-Aldrich (São Paulo, Brazil).

The cationic thermal initiator, Ytterbium (III) trifluoromethanesulfonate (YTT, Figure 1b), eugenol, phosphorus oxychloride ($POCl_3$), and Triethylamine (Et_3N) were purchased from Sigma-Aldrich. All substances were used as received.

The biobased transesterification catalyst, the Eugenol-based phosphate ester (EUGP) visible in Figure 1c, was synthesized following the procedure reported in the literature [45]. Recycled carbon fibers (RCF) were recovered from dismissed composite parts by mechanical milling, performing 10 milling cycles at 3000 rpm with a sieve size of 2 mm using a Pulverisette 19 equipment from Fritsch. SEM images of fillers are visible in Figure 1d.

2.1.1 | Epoxidation of Castor Oil

The castor oil was epoxidized following a procedure described in literature [46]. The ratio between mol of alkenes, H2O2, and acetic acid was 1:6:1. The amberlite IR-120 was used as a heterogeneous catalyst as 10 wt.% of the mass of CO.

The CO (50.0 g), H2O2 (58.0 mL), acetic acid (12.0 mL), and amberlite IR-120 (5.0 g) were added to a round-bottomed flask along with a magnetic bar.

The castor oil was epoxidized following a procedure described in literature [46]. The ratio between mol of alkenes, H_2O_2, and acetic acid was 1:6:1. The amberlite IR-120 was used as a heterogeneous catalyst as 10 wt.% of the mass of CO.

The CO, H_2O_2, and acetic acid were added to a round-bottomed flask along with a magnetic bar. The round-bottomed flask was

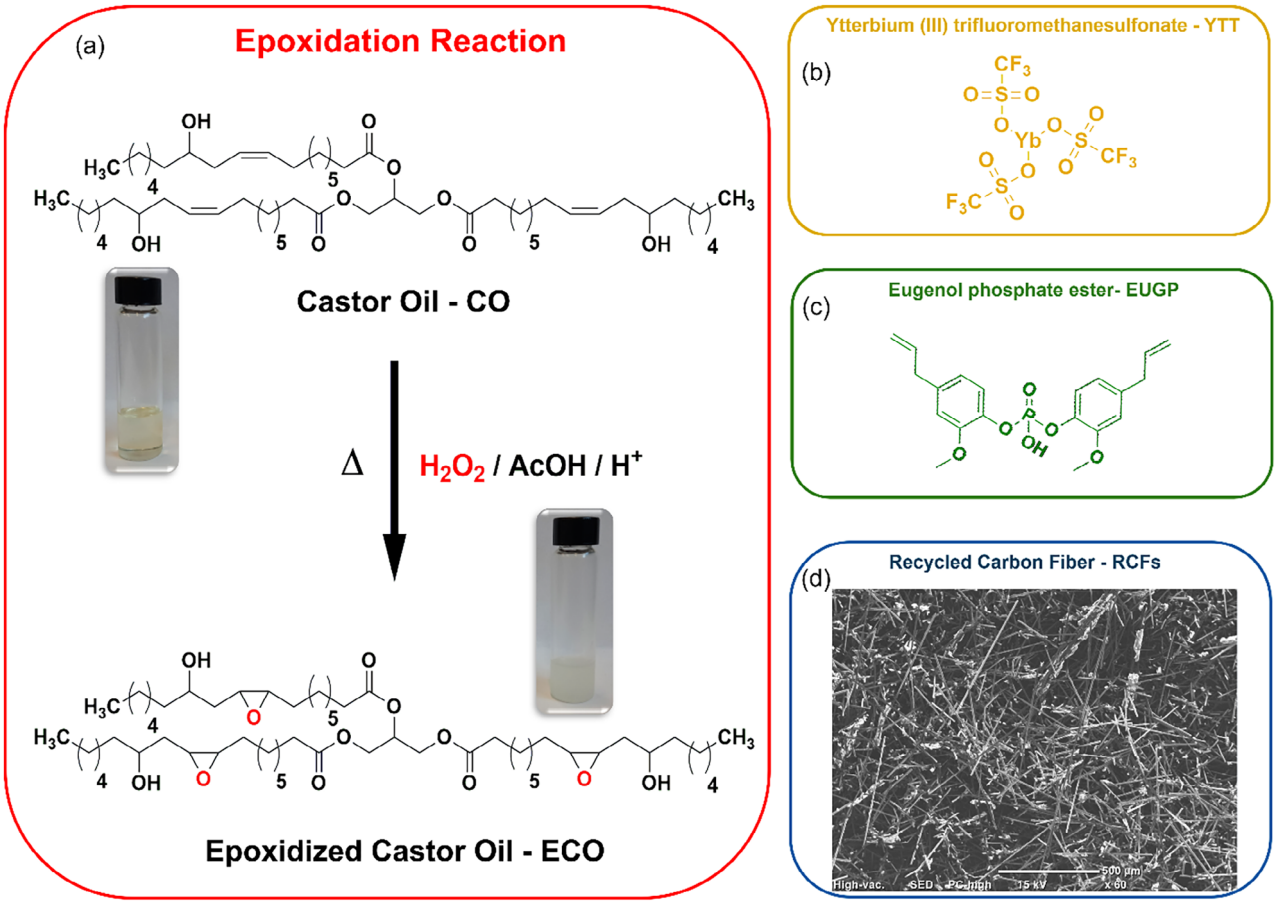

FIGURE 1 | (a) Epoxidation reaction and chemical structures for CO and ECO, (b) cationic thermal initiator, (c) biobased transesterification catalyst, and (d) SEM micrograph of Recycled Carbon Fiber.

attached to a distillation apparatus and settled in a heating mantle and heated up to 60 °°C. The reaction was maintained in this temperature for 3 h under stirring. Thereafter, the product was cooled down at room temperature and filtered to remove the catalyst, then the crude product was added to a separatory funnel together with ethyl acetate. The organic phase was washed with a sodium hydrogen carbonate solution (0.1 mol L^{-1}) to remove residual acid and then with brine, assisting the organic phase separation. After that, the organic phase was dried with magnesium sulfate and filtered to remove the desiccant compound. Finally, the ethyl acetate was removed from the product by using a rotary evaporator, then given the final product, a colorless viscous product when warmed, but a white paste material (epoxidized castor oil, ECO – Figure 1-a) at room temperature.

CO was characterized by ^{1}H-NMR to determine the iodine value (IV), amount of alkene per 100 g of samples, and the average number of alkenes ($DB_{average}$). Therefore, the CO was solubilized in $CDCl_3$ (containing TMS) and analyzed in an Agilent 400 MHz Premium Shield spectrometer (Bruker, Billerica, USA).

The IV for CO was determined by Equation 1, in which K is the sum of integrations from the multiplet between 5.30 ppm and 5.44 ppm and the double triplet at 5.55 ppm. These signals are related to vinyl hydrogens present in the fatty chain. The number of alkenes per 100 g of oil (mol) was easily determined by dividing the IV by the molar mass of I_2 (253.808 g mol^{-1}). The $DB_{average}$ was determined by Equation 2, the Nf is associated with four hydrogens attached to the glycerol backbone (4.14 ppm and 4.29 ppm) divided by the number of related hydrogens (4 hydrogens) [46].Before any integration, the signal was normalized by the area at 2.31 ppm (triple doublet), which is related to six hydrogens atoms of the α-carbonyl in the fatty chain.

The epoxidized castor oil (ECO) was also characterized by ^{1}H-NMR following the above procedure. By the ^{1}H-NMR spectrum, it was possible to determine the epoxy conversion by monitoring the vinyl hydrogens.

$$IV = \frac{(12691 \times K)}{(821.3 + 6.006 \times K)} \quad (1)$$

$$DB_{average} = \frac{K}{2Nf} \quad (2)$$

The epoxy oxygen content in the epoxidized castor oil was measured using a standard titration method for epoxy resin epoxide content (ASTM D1652, 2019). This method was executed in triplicate and involves the reaction between TEAB and perchloric acid ($HClO_4$, 0.116 mol L^{-1}), which produces hydrogen bromide (HBr) in situ. As a result, HBr reacts in a 1:1 ratio with the epoxide ring, forming a bromohydrin. The mass of the ECO used was approximately 200 mg. The endpoint was determined when an excess of acid was formed, resulting in a color change from violet

to yellow-greenish, since violet crystal was used as an acid-base indicator.

2.1.2 | Adhesive Formulation Preparation

A total of 3 adhesive formulations have been studied, based on the amount of filler, pristine, 10 phr and 20 phr RCF. In each formulation, 2 phr of YTT-cationic thermal initiator, and 15 phr EUGP-biobased transesterification catalyst, were added, based on previous studies [43, 45, 47].

For all the formulations, THINKYMIXER ARE-250 planetary mixer was used to distribute fillers in the biobased precursor homogeneously and degas the formulations, according to the following program: 1 min mixing and then 1 min degassing at 1600 rpm, 1 min mixing and then 1 min degassing at 1800 rpm, and finally 2 min mixing at 2000 rpm.

2.2 | Joint and Sample Manufacturing

The process to manufacture the joints involved the application of the resin on the surface of the substrates and then covering with the second piece of metal or composite.

Two different substrates were tested, a ceramic matric composite (CMC), SiC/SiC (C fiber reinforced Si/SiC matrix, random short fibers) a metallic based material, Al alloy (precipitation-hardened Al alloy EN AW-6082 T6). Similar joints, CMC to CMC (CMC/CMC), and Al alloy to Al alloy (Al/Al) joints have been produced, at least 5 joints for each formulation and for each curing treatment.

The substrates were cut into rectangular specimens with dimensions of 25 × 12.5×5 mm. They were bonded using ECO adhesives, with an area of 25×5 mm, arranged in a tensile test configuration to conform to the test set-up. The adhesive layer thickness ranged between 150 and 200 µm. Prior to bonding, the substrate surfaces were polished to ensure uniform contact with the adhesive. The polishing was carried out using a grinding machine equipped with 400-grit sandpaper, and subsequently, the specimens were cleaned in an ultrasonic bath with acetone for 30 min.

Once the liquid formulation was correctly deposited and the two substrates were correctly positioned, the samples were left in an oven at 90 °°C for 1h to undergo the curing process. The joined area is 125 mm^2.

DMTA, tensile and stress-relaxation adhesive samples were produced by pouring the liquid formulation into silicon molds and then undergoing the curing processes previously explained. 5 samples for each formulation and curing processes have been produced, with dimensions of 18×8×1 mm^3 for DMTA, dumbbell shape in accordance with ISO527A-5B standard for tensile tests, and discs of 10 mm in diameter and 0.5 mm in thickness for stress-relaxation analysis.

To reduce the environmental footprint of the process, a parallel set of specimens was cured at room temperature (25 °°C, 24 h), avoiding oven heating and allowing to quantify the performance trade-off of this low-energy route. In particular, FTIR conversion analysis, gel content, and DMTA were carried out on these samples.

2.3 | Characterizations of Curing Process

2.3.1 | Differential Scanning Calorimetry

The DSC analyses were performed using a Mettler Toledo DSC-1 instrument under a nitrogen atmosphere, with a flow rate maintained at 40 mL min^{-1}. Three samples of each formulation were analyzed to calculate a weighted average while considering the standard deviation of the obtained values.

For the measurements, 5–10 mg of liquid formulation was placed in an aluminum crucible with a capacity of 40 µL, while an empty crucible served as the reference. The heating programs were conducted in the temperature range of 25–180 °°C, with a heating rate of 3 K min^{-1}. Specific heat flow curves [W g^{-1}] were recorded as a function of temperature [°°C]. The peak height is directly related to the polymerization rate, with higher values indicating faster polymerization kinetics. The enthalpy change (ΔH) was determined by integrating the area under the heat flow curve.

To evaluate the thermodynamic properties of the curing process, dynamic DSC experiments were conducted to assess the best curing temperature.

Isothermal DSC was employed to assess the curing behavior of the formulations at a constant temperature of 90 °°C, which was previously identified as optimal through dynamic DSC. Unlike dynamic scans, which vary temperature over time, isothermal analysis allows the evaluation of reaction kinetics under controlled thermal conditions, isolating the effect of time on the curing process. This approach is particularly useful to confirm whether curing proceeds efficiently and completely at the selected temperature. Additionally, it enables direct comparison between different formulations, highlighting how increasing the amount of recycled carbon fibers (RCF) affects the rate and extent of curing.

The enthalpy released during complete crosslinking of the sample, ΔH_{tot} [J g^{-1}], was calculated using Equation 3.

$$\Delta H_{tot} = n \cdot f \cdot H_{ep} \cdot \frac{1}{PM} \tag{3}$$

where, n is the number of epoxy rings per mole of monomer; f is the fraction of epoxy groups involved in network formation rather than side reactions ($f = 1$ in this work), H_{ep} corresponds to the theoretical enthalpy of epoxy ring opening [J mol^{-1}] (equal to 74 kJ mol^{-1}, exothermic), and PM is the monomer's molecular weight [g mol^{-1}], calculated as 975 g mol^{-1} for ECO.

Integration of Equation (3) yields the conversion percentage (C), as shown in Equation 4 [48, 49].

$$C = \frac{1}{\Delta H_{tot}} \cdot \int_0^t \left(\frac{dH}{dt}\right)_T \tag{4}$$

where $(dH/dt)_T$ denotes the heat flow measured under isothermal conditions (90 °°C) [J g $^{-1}$ s^{-1}].

Three measurements were performed for each sample type.

2.3.2 | FT-IR

IR spectroscopy was used to measure the conversion of the resin upon thermal curing. In particular, a lowering of the peak characteristic of epoxies after curing is expected. The conversion was calculated using Equation 5 [48, 49].

$$Conversion\,(\%) = \frac{\left(\frac{A_{functional}}{A_{reference}}\right)_{t=0} - \left(\frac{A_{functional}}{A_{reference}}\right)_{t}}{\left(\frac{A_{functional}}{A_{reference}}\right)_{t=0}} \cdot 100 \quad (5)$$

where $A_{\text{functional}}$ is the peak area of the functional group under investigation during the test, specifically the epoxy group (centered at 842 cm^{-1}), and $A_{\text{reference}}$ is the area of the peak used as a reference, the carbonyl one in this case, centered at around 1780 and 1680 cm^{-1} [50]. With t = 0 and t, the pre- and post-thermal energy exposure times are indicated, respectively.

The Thermo ScientificTM NicoletTM iS50 FT-IR spectrometer and OmnicTMSpectra software were used to conduct this analysis; the oven used to perform the thermal curing is ArgoLab TCN30 Plus. The formulations were deposited on a silicon substrate with a spreader bar, in the form of films approximately 12 μm thick. Subsequently, the IR spectrum of the test sample was recorded prior to thermal exposure (pre-curing, t = 0 min). After that, each film was inserted in the oven at 90 °°C for 1 to 120 min. After each curing step, the IR spectrum of the sample was again recorded by noting the irradiation time, t (min). In a second period, the conversion percentage of the samples is calculated and reported as a function of time.

The same procedure was used to conduct conversion analysis on ambient-cured samples. The 12 μm thick film was left at ambient temperature (25 °°C) and spectra were recorded after 1, 3, 6, 12, 24, and 36 h. Conversion curves were calculated from FT-IR spectra.

2.4 | Characterizations of Cured Adhesives

2.4.1 | Gel Content

The gel content (%gel) analysis was carried out by measuring the weight loss of cured samples (approximately weight 150–200 mg in weight) after immersing them in chloroform for 24 h at room temperature. Following the immersion, the samples were dried for 24h in air at room temperature, with an additional drying step at 60 °°C for 6 h to eliminate any remaining solvent. The insoluble fraction was calculated using Equation 6. All tests were conducted in triplicate for each composite.

$$\%gel = \frac{W_1}{W_0} \cdot 100 \quad (6)$$

2.4.2 | DMTA

The Dynamic Mechanical Thermal Analysis (DMTA) was conducted using the Triton Technology instrument (Tritec 2000) in tension mode with the application of a uniaxial stress, with a frequency of 1 Hz and a heating rate of 3 °°C min^{-1}. Tests were conducted using liquid nitrogen to cool the chamber to approximately −60 °°C and were terminated when the rubbery plateau was reached, at 80 °°C. The glass transition temperature (T_g) was taken as the maximum of $tan\delta$ (TanDelta) curves.

The crosslinking density, ν_c [mol m^{-3}], of the samples was evaluated using Equation 7.

$$\nu_C = \frac{E'}{3RT} \quad (7)$$

where E' is the storage modulus in the rubbery plateau [Pa], registered at temperature T = Tg + 50 °°C, expressed in K, and R is the gas constant (8.314 J K^{-1} mol^{-1}).

2.4.3 | Contact Angle

The contact angles for all cured materials were measured using a Kruss DSA10 tensiometer (Krüss Scientific, Hamburg, Germany) equipped with a digital camera. A drop of water was deposited on the surface of each sample, and 10 optical scans were performed to verify the contact angle formed between the drop and the surface. This method was executed in triplicate.

2.4.4 | TGA

Pristine crosslinked ECO was subjected to thermogravimetry (TGA) using a Mettler-Toledo TGA/DSC 3$^+$ Star^e System module. The sample (9.0 mg) was placed into an α-alumina open crucible (200 μL). The temperature range was from 30 °°C to 800 °°C in a heating rate of 10 °°C min^{-1} under a dynamic dry air atmosphere (40.0 mL min^{-1}).

2.4.5 | Stress-Relaxation Analysis

Stress relaxation behavior of the crosslinked adhesives was determined using a MCR 501 rheometer from Anton Paar. The sample had an average dimension of 0.5 mm × 1 mm diameter. The sample was first preloaded with a normal force of 10 N applied for 15 min at the set temperature, then a constant 3% strain was applied, and the variation of the relaxation modulus was recorded over time. The chosen temperatures corresponded to 70 °°C, 80 °°C, 90 °°C, and 100 °°C.

The relaxation modulus $G(t)$ was normalized by the initial value G_{t0}. The characteristic relaxation time was determined as the time needed by the normalized modulus to reach *1/e*, with an exponential decrease following Equation 8.

$$G\,(t) = G_{t0}e^{-\frac{t}{\tau}} \quad (8)$$

where τ is the relaxation time [s].

The activation energy was extrapolated from the Arrhenius plot, considering Equation 9:

$$\ln(\tau) = \ln(\tau_0) + E_a \frac{1}{RT} \quad (9)$$

where E_a is the activation energy [J mol^{-1}], R is the universal gas constant [J mol^{-1}K^{-1}], T is the temperature [K], and τ_0 is a pre-exponential factor. By plotting $\ln(\tau)$ vs. $1000/T$, it is possible to calculate Ea using Equation 10, considering the slope of the curve (a).

$$E_a = a \times 1000 \times R \quad (10)$$

2.4.6 | Tensile Test

The tests were conducted at room temperature on joints in a tensile instrument (MTS QTestTM/10Elite) from MTS System Corporation, with a translation speed of 2 mm^{-1} and a loading cell of 5 kN for both mechanical tests on the materials themselves and on joints.

At least 5 samples were tested for each similar joint and the results of the mechanical tests were expressed as mean ± standard deviation.

3 | Results

3.1 | Castor Oil Epoxy Functionalization

The starting biobased precursor exploited in this work was an epoxidized castor oil achieved by epoxidation reaction, as reported in Figure 1a.

The starting CO presents 0.4137 mol of alkenes per 100 g (C = C) measured by ^{1}H-NMR. The $DB_{average}$ was equal to 3.6 units of alkene per molecule; therefore, the triacylglycerol for this oil is not composed only of the ricinoleic chain. In a pure ricinoleic chain structure, the $DB_{average}$ would be equal to 3 units. In the ^{1}H-NMR spectrum reported in Figure 2a, the signal at 3.61 ppm is related to hydrogen attached to the carbinolic carbon in the ricinoleic chain; in addition, two other signals can be observed related to the α-linolenic chain. These signals appear as a triplet at 0.98 ppm associated with methyl hydrogens at the end of the chain and a triplet at 2.77 ppm related to bis-allylic hydrogens [46, 51, 52].

After the epoxidation reaction, the multiplet between 5.30 ppm and 5.44 ppm and the double triplet at 5.55 ppm related to vinyl hydrogens vanished, just remaining the quintuplet at 5.26 ppm related to the hydrogen attached to the secondary carbon of the glycerol backbone [46, 51, 52]. Therefore, by the ^{1}H-NMR spectrum for ECO, Figure 2b, the conversion was >99%, and new signals related to hydrogens attached to epoxy carbon appear at 2.94, 3.13, and 3.41 ppm [46].

The epoxy oxygen content in ECO was 6.11±0.57 wt% of oxygen. Therefore, 100 g of ECO contains 6.11 g of oxygen. Dividing this value by the atomic mass of oxygen (16 Da) allows calculation of the molar amount of epoxy rings, which is 0.3820 ± 0.015 mol. Comparing this value with the mol of alkenes (0.4137 mol) gives us the percentage of epoxy rings present in 100 g of ECO, which is 92.35±3.64%. Although the ^{1}H-NMR shows a conversion of greater than 99%, the epoxy amount indicates that some rings may have opened during the synthesis.

3.2 | Curing Analysis

The curing behavior of epoxidized castor oil formulations using 2 phr of YTT as a thermal initiator, with varying contents of RCF, was evaluated by DSC analysis, and the heat flow curves are reported in Figure 3. The pristine formulation exhibited a distinct exothermic peak at approximately 95 °°C, indicative of the maximum curing rate. Incorporating 10 phr RCF slightly shifted the peak to lower temperatures, around 92 °°C, suggesting that the addition of fibers modestly enhances the curing kinetics, possibly attributable to the enhancement of thermal conductivity imparted by the dispersed fibers. Further increasing the fiber content to 20 phr RCF resulted in a more pronounced shift of the exothermic peak toward lower temperatures, approximately 85 °°C, clearly demonstrating that higher concentrations of recycled carbon fibers significantly accelerate the curing process. Additionally, increasing the RCF content led to broader exothermic peaks, indicating a more heterogeneous curing reaction due to fiber-induced changes in heat transfer and reaction dynamics. Overall, the presence of recycled carbon fibers positively impacts curing kinetics by reducing the onset and peak temperatures, thus allowing lower-temperature processing conditions.

Based on the dynamic DSC analysis, the optimal curing temperature of 90 °°C was selected, and isothermal DSC analysis was subsequently carried out at this temperature. As visible in Figure 4, the pristine formulation displayed a rapid exothermic reaction, reaching a maximum heat flow of approximately 2.2 W g^{-1} within the first 50 s. Formulations with 10 phr and 20 phr RCF showed reduced peak heat flows of around 1.2 W g^{-1} and 0.9 W g^{-1}, this is due to a lower resin content with respect to the sample weight due to the presence of the fibers. In fact, the reduction in exothermicity with increasing RCF content can be attributed to a dilution effect, as fibers replace a portion of reactive resin, and enhance thermal conductivity of carbon fibers, which improves heat dissipation within the composite, thereby reducing the intensity of the exothermic reaction. All formulations approached a similar final heat flow after approximately 300 s, demonstrating that the overall extent of curing was not significantly hindered by the addition of recycled carbon fibers. Table 2 reports enthalpy [J g^{-1}] values and conversion [%] for the studied formulations.

The curing behavior of epoxidized castor oil formulations was quantified also by FTIR spectroscopy, following the decrease of the epoxy ring deformation band at ≈ 830 cm^{-1} [53]. As an example, the FT-IR spectra of ECO with 20 phr RCF cured at 90 °°C are reported in Figure 5a.

In Figure 6a, the conversion curves as a function of time are reported for all the formulations investigated. It is possible to observe that epoxy conversion increased steeply during the first 30 min and then leveled off. As reported in Table 2, pristine ECO reached 88 ± 1%, the formulation containing 10 phr RCF a final

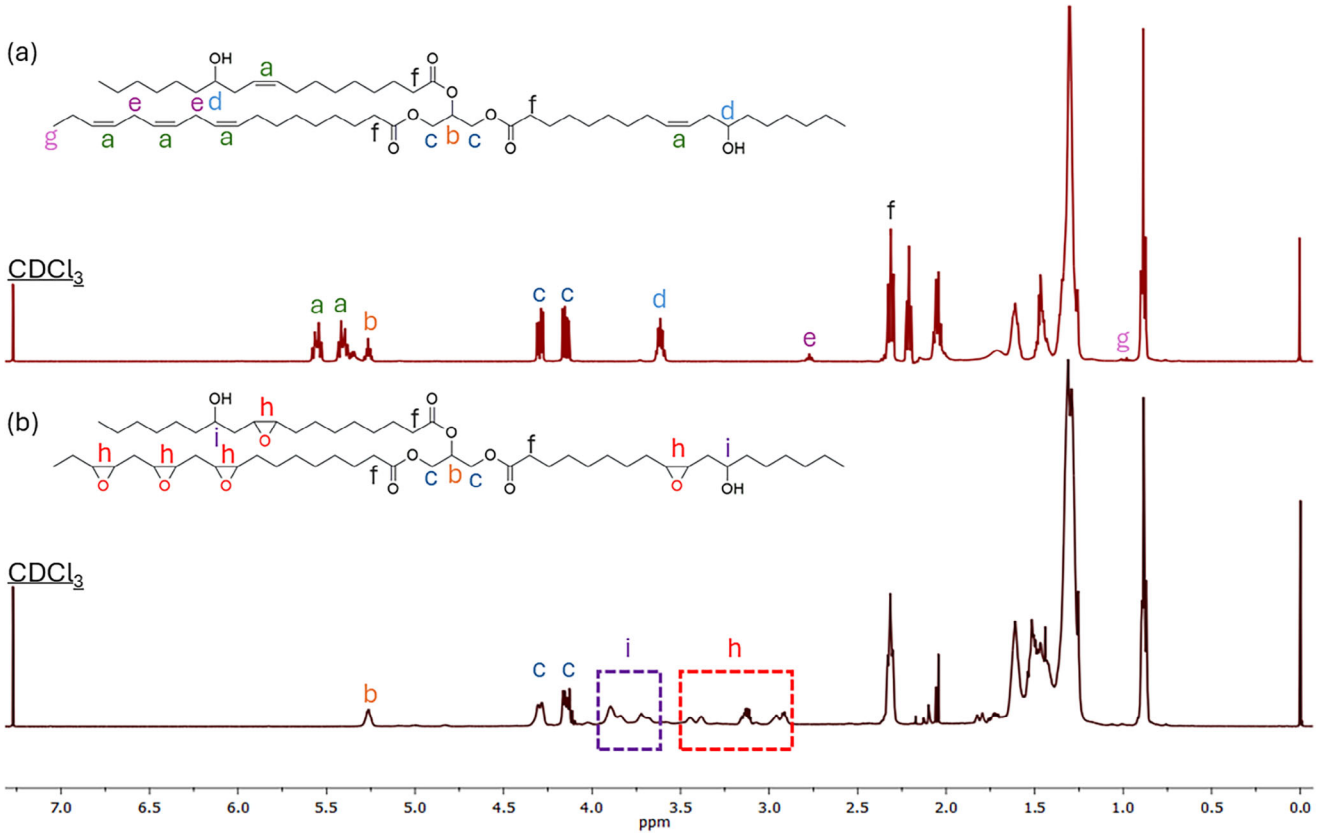

FIGURE 2 | ^{1}H-NMR spectra for (a) CO, and (b) ECO.

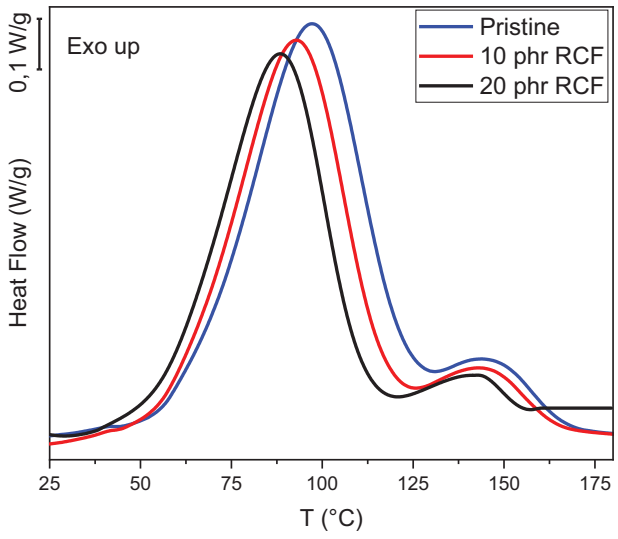

FIGURE 3 | Dynamic DSC curves of all the studied formulations.

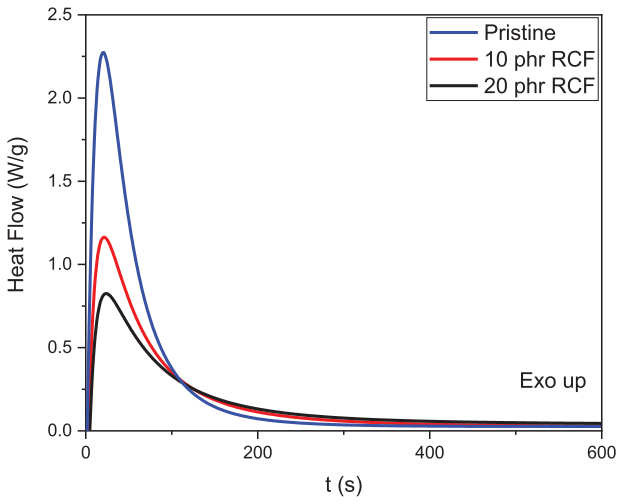

FIGURE 4 | Isothermal DSC (90 °°C) curves of all the studied formulations.

conversion of 86 ± 1%, and the formulation containing 20 phr RCF 82 ± 2%. The modest drop in final conversion by increasing the fiber content in the formulation can be attributed to steric and diffusion constraints imposed by the rigid RCF network, which hampers chain mobility and the approach of reactive centers [54].

In order to evaluate the possibility of proceeding with a room temperature curing process, to reduce environmental impact, the FTIR analyses were followed over a longer time leaving the formulations at room temperature.

In Figure 5b the FT-IR spectra of ECO with 20 phr RCF cured at 25°°C, measured at 0h, 12 h, 24h and 36 h, are collected.

The conversion curves as a function of time are reported in Figure 6b for all the investigated formulations cured at 25°°C. After 36 h the epoxy conversion was on a plateau at respectively

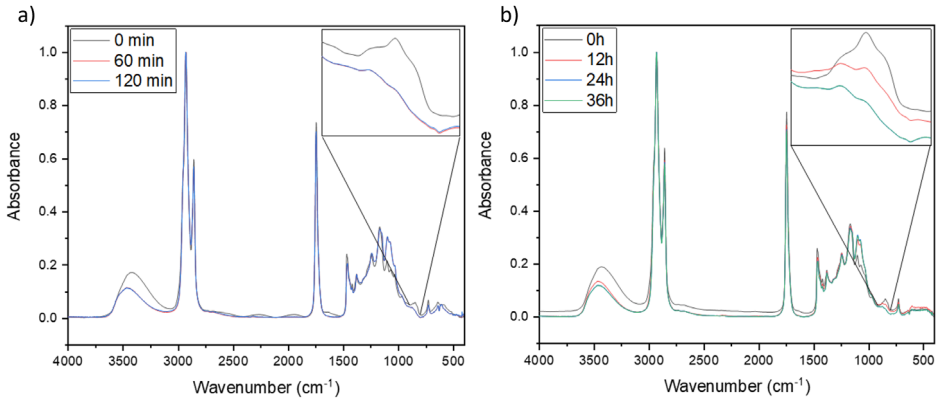

FIGURE 5 | FT-IR spectra of ECO with 20 phr RCF cured at 90°°C (a) and 25°°C (b), reported at different curing times.

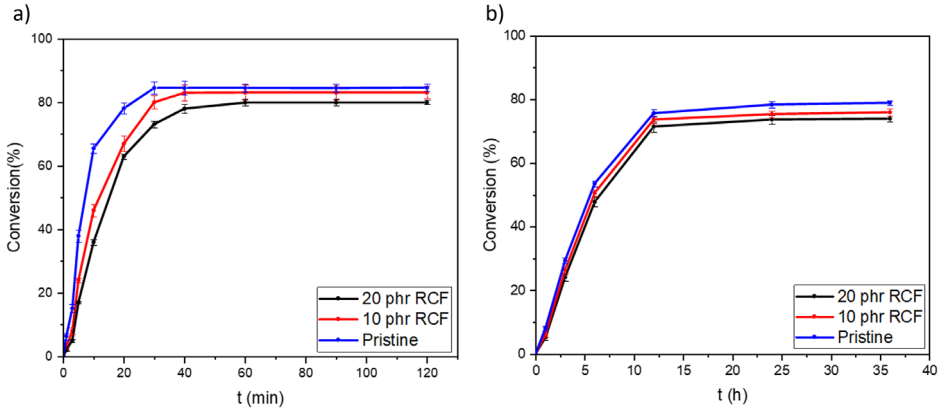

FIGURE 6 | FT-IR conversion curves of formulations cured at 90°°C (a) and 25°°C (b).

78 ± 1% for the pristine formulation, 76 ± 1%, for the formulation containing 10 phr RCF and 74 ± 2%, for the formulation containing 20 phr RCF

The ambient temperature curing can be explained considering the initiator added to the formulation, the ytterbium(III) triflate [$Yb(OTf)_3$]. In fact, this salt is a highly oxophilic, water-tolerant Lewis acid that can activate epoxides by coordinating to the ring oxygen, thereby generating a carbocation species that propagates via an activated-monomer mechanism. Its catalytic activity persists in humid environments because the triflate ligands stabilize the Yb^{3+} center, preventing hydrolysis [55]. Detailed calorimetric studies have shown that $Yb(OTf)_3$ lowers the apparent activation energy for epoxy homopolymerization to ≈ 85 kJ mol^{-1} and can initiate cure well below 50°°C [56]. In the ECO system, this translates into significant polymerization even without external heating; elevation to 90°°C merely accelerates a reaction that is already thermodynamically accessible.

Gel content values, reported in Table 1 show that every formulation, independently of the two studied curing processes, is essentially insoluble, confirming the formation of a permanent 3D network.

In fact, for the samples obtained with a high temperature cure (90°°C, 1 h), gel contents were around 99.8% for pristine ECO, 99.2% for the 10 phr RCF composite, and 98.9% for the 20 phr RCF composite.

Meanwhile, for the samples obtained at ambient cure (25°°C, 24 h) the measured gel contents were 99.1% for the pristine sample and 98.9% and 98.7% for the crosslinked samples containing 10 phr and 20 phr RCF, respectively. Showing similar gel content values and demonstrating the cure efficiency also at room temperature for the investigated formulations.

Table 1 summarizes the curing behavior and network formation of the studied formulations.

In general, a gradual decrease in the total reaction enthalpy is observed with increasing RCF content, indicating that the introduction of RCF slightly reduces the number of reactive epoxy sites available for crosslinking. This reduction can be attributed to physical restriction due to the interaction between RCF and the epoxy matrix, which may limit the mobility of the reactive species during curing. The conversion degrees determined by DSC and FTIR follow a similar trend: the pristine system exhibits the highest curing efficiency, whereas the formulations containing 10 and 20 phr of RCF show progressively lower conversions. This suggests that the filler acts as a diffusion barrier, slowing down the reaction kinetics and hindering crosslinking.

Despite these effects, as already said, the gel content remains very high for all samples (>98%), both for room temperature and 90°°C curing. This indicates that a continuous and stable polymer network is formed in every formulation. The slightly lower gel content in systems containing RCF likely reflects the

TABLE 1 | Enthalpy, DSC and FTIR conversions, and Gel content of the studied formulations.

Type	ΔH_{tot} [J g^{-1}]	DSC conv [%] @90°°C	FTIR conv [%] @90°°C	FTIR conv [%] @r.t.	Gel content [%] @90°°C	Gel content [%] @r.t.
Pristine	130±3	70±1	88±1	78±1	99.8±0.2	99.1±0.1
10 phr RCF	125±5	68±2	86±1	76±1	99.2±0.1	98.9±0.1
20 phr RCF	121±4	65±2	82±2	74±2	98.9±0.2	98.7±0.1

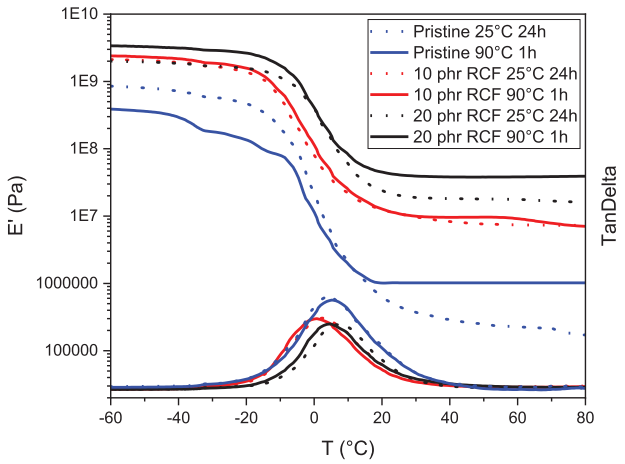

FIGURE 7 | Storage modulus (E') and TanDelta peaks of the studied formulations cured at ambient and high temperature.

small fraction of unreacted species trapped within the filler-rich regions rather than incomplete network formation.

3.3 | DMTA Analysis of the Crosslinked Adhesives

The crosslinked formulation adhesives were investigated by DMTA analysis to demonstrate viscoelastic properties within the temperature range. In Figure 7 the E' and *tanδ* curves are reported for the investigated adhesive formulations, both cured at room temperature and at 90°°C.

As evident from the DMTA curves, in the rubbery-plateau region, the storage modulus (E′) of the pristine epoxy crosslinked adhesive remains at around 1 MPa, indicating a low load-bearing capacity. Introducing RCF at 10 phr in the curable formulation elevates E′ in this regime to about 10 MPa, and a further increase of the fibers content to 20 phr nearly quadruples that, to approximately 40 MPa. The stiffening effect reflects the formation of a percolated fiber skeleton. Above *Tg* the rigid fibers become the principal load-bearing phase, with stress transferred efficiently through fiber–fiber contacts and across a well-adhered interphase to the surrounding matrix. Curing at 90°°C for 1 h yields a consistent secondary enhancement in rubbery modulus, due to a higher effective cross-link density that tightens the network and reduces viscous relaxation pathways.

The glass-transition temperature, determined from the maximum of *tanδ* peak, follows a non-linear trend with filler loading: the pristine crosslinked resin has a *Tg* of roughly 6°°C, the cured formulation containing 10 phr fiber content showed a *Tg* around 0°°C, likely because moderate fiber content interferes with network development and creates localized regions of lower crosslink density, and the *Tg* of the crosslinked adhesive formulation containing 20 phr fiber content showed a *Tg* of about 6°°C as the percolating fiber network imposes greater segmental restriction the reinforcement effect is evident.

Finally, the curing temperature has a negligible effect on *Tg*, with transition temperatures remaining effectively unchanged between room temperature and elevated temperature cures.

In addition, Table 2 reports the crosslinking density values derived from the storage modulus registered in the rubbery plateau, E' (Tg+50°°C).

The data reported in the table clearly show how both the fiber content and the curing temperature affect the stiffness and structure of the network.

For the pristine material, the crosslink density indicates a relatively loose polymer network since it's characterized by the lowest values. When 10 phr of RCF are added, ν_c increases by one order of magnitude, and at 20 phr it reaches the maximum values. This trend follows the increase in E′ observed in the rubbery region and confirms that the presence of the fibers promotes a more constrained network. The formation of a continuous fiber skeleton allows stress to be transferred more efficiently through the composite, restricting the motion of the surrounding matrix.

The comparison between the two curing procedures shows that samples cured at 90°°C for 1 h consistently reach higher values of E′ and ν_c than those cured at room temperature for 24 h. The curing at high temperature likely drives additional crosslinking reactions, as already reported in the curing analysis via FTIR and gel content, tightening the polymer network and reducing chain mobility.

In summary, both the amount of RCF and the curing temperature play a decisive role in reinforcing the polymeric network, with the fibers acting as the main contributors to increase stiffness, and the high temperature curing ensuring a denser network and better crosslinked structure.

3.4 | Mechanical Properties of the Crosslinked Adhesives

The stress–strain curves of the investigated crosslinked adhesives, reported in Figure 8, show a clear, monotonic improvement in tensile performance as the RCF content is raised from 0 to 20 phr. As visible from Table 3, the crosslinked pristine ECO has a Young's modulus of 190±6 MPa, the maximum stress reaches

TABLE 2 | Storage modulus in the rubbery plateau and crosslinking density of all the studied samples, considering both the curing procedures.

Type	E′(Tg + 50°C)@90°°C [MPa]	E′(Tg + 50°C) @r.t. [MPa]	ν_c @90°°C [mol m^{-3}]	ν_c @r.t. [mol m^{-3}]
Pristine	1.1±0.6	0.2±0.1	124±68	28±14
10 phr RCF	9.5±1.2	7.5±1.0	1179±149	930±124
20 phr RCF	38.4±3.1	18.3±2.3	4629±374	2193±276

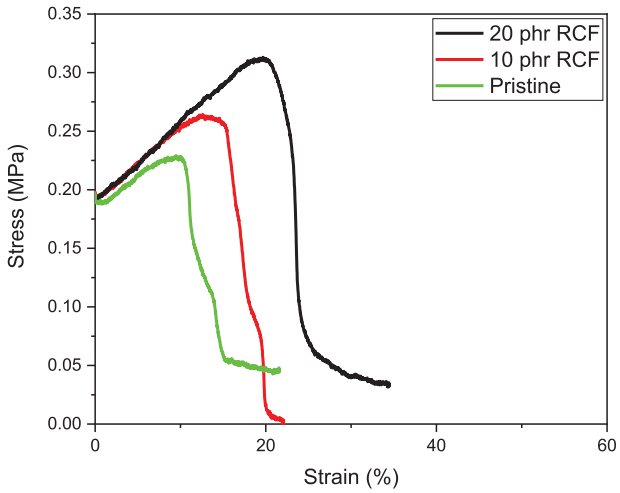

FIGURE 8 | Stress vs Strain curves of the studied materials.

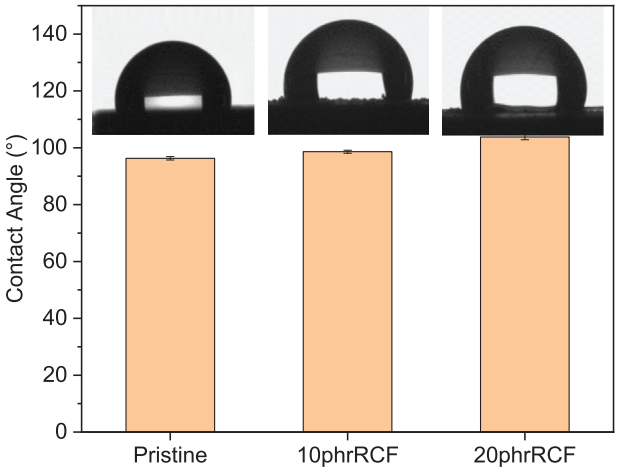

FIGURE 9 | Contact angle values of the studied materials.

TABLE 3 | Mechanical properties of the bulk materials.

Sample	Young's modulus [MPa]	Peak Stress [MPa]
Pristine	190±6	0.22±0.09
10 phr RCF	200±4	0.26±0.05
20 phr RCF	220±5	0.31±0.04

0.22±0.09 MPa at around 11% strain. Adding 10 phr RCF to the adhesive formulation an enhancement of stiffens of the initial slope to 200±4 MPa, lifts the tensile strength to 0.26±0.05 MPa at around 17% strain, which is evident attributable to a stress transfer across a well-bonded fiber–matrix interface. When the fiber content is increased to 20 phr the reinforcement becomes much more pronounced, the modulus approaches 220±5 MPa, the peak stress climbs to 0.31±0.04 MPa at much higher strain, around 22%. The area under the curve, an indicator of work-to-fracture, therefore more than doubles relative to the pristine crosslinked resin. These trends confirm that a progressively denser fiber skeleton not only carries a larger share of the applied load but also redistributes stresses through fiber–fiber contacts, delaying instability and enhancing both strength and ductility without sacrificing toughness.

3.5 | Contact Angle

Static water contact-angle measurements supply complementary information on the outermost molecular layers of the cured films (90°°C, 1h). As visible in Figure 9, the pristine crosslinked ECO surface displayed a contact angle around 95°, indicative of a moderately hydrophobic matrix. Progressively increasing the recycled-carbon-fiber content in the curable formulation, produced a monotonic rise of the cured adhesive to 98° for the formulation containing 10 phr RCF composite and to a value of 105° for the formulation 20 phr RCF.

Two synergistic factors account for this trend: the intrinsically low surface energy of graphitic carbon, which lowers the overall polarity when fiber ends or micro-protrusions become exposed at the air interface, and an increase in microscale roughness introduced by partially emergent fibers, which amplifies the apparent contact angle according to Wenzel/Cassie–Baxter wetting models [57, 58].

The curing mechanism doesn't affect contact angle values.

3.6 | TGA

Thermogravimetric analysis of pristine crosslinked ECO was measured, and the TGA curve is reported in Figure 10, showing that the material is thermally robust up to about 250°°C, retaining more than 95% of its mass. Between 105°°C and 250°°C, two steps of mass loss overlap in the TG, however, they are visible by DTG. The first event, near 105°°C, could be due to evaporation of residual moisture. The second, at 250°°C, likely arises from acid-catalyzed decomposition promoted by YTT. From 250°°C to 490°°C the derivative curve reaches its most negative value, indicating the fastest rate of mass loss, which is attributed to the main degradation process of polymeric matrix-scission of the epoxidized triglyceride backbone. Hence, the carbonaceous matter is formed and further reacts with O_2 to cause combustion

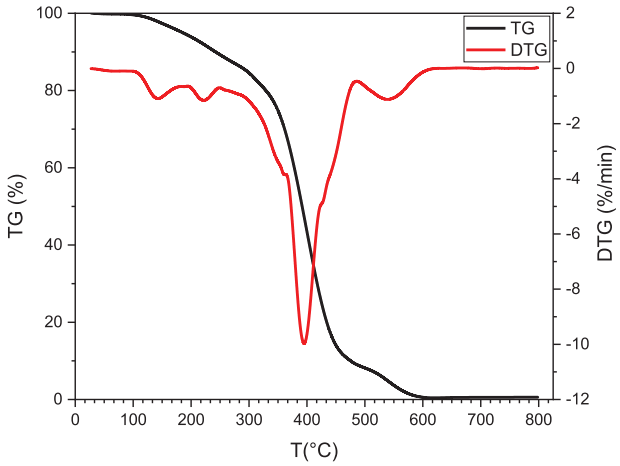

FIGURE 10 | TG and DTG of pristine ECO.

and degradation processes. This process occurs between 490°°C and 610°°C.

The TGA results were used to define the temperature window for subsequent stress-relaxation experiments. Test points were chosen well inside the safe region, with the highest set at 100°°C. Operating at this maximum temperature provides a meaningful acceleration of viscoelastic relaxation while remaining more than 200°°C below the onset of major thermal degradation, ensuring that any observed mechanical changes can be attributed to molecular mobility rather than chemical breakdown.

3.7 | Stress-Relaxation Analysis

The stress-relaxation behavior of the crosslinked formulations based on ECO was evaluated at four different temperatures: 70°°C, 80°°C, 90°°C, and 100°°C as reported in Figure 11. These temperatures were selected to ensure thermal activation of the exchange mechanism while avoiding degradation of the polymer matrix, based on the TGA data. As expected for covalent adaptable networks governed by associative bond-exchange reactions, all formulations exhibited a progressive acceleration of the relaxation process with increasing temperature. Notably, at 100°°C, the normalized relaxation modulus of each system decayed to the *1/e* threshold (dotted line) within the shortest time, confirming the thermally activated nature of the transesterification process catalyzed by the biobased phosphate ester.

The characteristic relaxation times (τ) were extracted from each relaxation curve. These values were then used to construct Arrhenius plots for the crosslinked pristine formulation as well as for the crosslinked formulations containing 10 phr and 20 phr RCF, as visible in Figure 12. In all cases, the data followed a linear trend, consistent with Arrhenius-type kinetics. The activation energies (*Ea*), derived from the slope of each linear fit, were calculated to be 108.1 kJ mol^{-1} for the unfilled system, and significantly lower values of 34.9 kJ mol^{-1} and 33.2 kJ mol^{-1} for the 10 phr and 20 phr RCF containing formulations, respectively. These results confirm that the addition of recycled carbon fibers facilitates the dynamic exchange process.

We suppose that the acceleration of stress relaxation with increasing RCF loading can by explained considering different factors. First, the fibers emerge from the recycling process with surfaces rich in hydroxyl, carbonyl and carboxyl groups, as well as trace transition-metal residues; these sites act as Brønsted- or Lewis-acid centers that catalyze the associative ester-alcohol exchange, directly lowering the intrinsic activation barrier of the transesterification step. Second, once the RCF content approaches percolation, the graphitic network improves heat distribution throughout the sample, so a more uniform temperature is reached during testing, which registers as a smaller apparent activation energy. Third, fiber interfaces disrupt the epoxy network, generating free volume that facilitates bond rearrangement. Fourth, the overall epoxy conversion after curing is slightly reduced as the filler fraction rises, which leaves a lower cross-link density and increases chain dynamics and reduces the energy cost of bond exchange.

3.8 | Mechanical Properties of the Joints

FESEM cross-sections of CMC and Al alloy joined with adhesive with 20 phr RCF are shown in Figure 13a,b, respectively. The bonding layer is uniform and dense, with a thickness < 200 μm, and the interfaces are continuous especially for CMC substrates, without cracks or pores, which indicates that the joint has the potential to exhibit bonding strength. Higher porosity is visible at Al alloy/adhesive interface. Good adhesion of the joining material with both surfaces (CMC and Al alloy) can be observed in all the joints, with or without RCF. At higher magnification, the composite/adhesive interface shows a more structured surface in comparison with Al alloy surfaces, due to the flow of the adhesive and its penetration of the composite fabric and of the porosities of the composite all along the irregular fiber surface.

Figure 14a shows the tensile stress–strain curves for CMC/CMC joints, whereas Figure 14b presents the plots for Al alloy/Al alloy joints. Table 5 report stresses [MPa] and retained strength [%] of CMC and Al alloy joints, respectively.

As visible from the tables, for both substrates, adding RCF to the adhesive formulation markedly increased the joint strength. On CMC joints the pristine formulation reached only 0.08 ± 0.01 MPa, but this value rises respectively to 0.13 ± 0.01 MPa and to 0.19 ± 0.02 MPa for the formulation containing 10 phr and 20 phr RCF. A similar ranking was obtained on Al alloy substrates, where the virgin strength increased from 0.05 ± 0.01 MPa (pristine) to 0.11 ± 0.01 MPa (10 phr RCF) and 0.14 ± 0.01 MPa (20 phr RCF). The mechanical values obtained are in line with the literature regarding not structural biobased crosslinked polymers on different substrates [59–64].

After the first tensile test on the virgin joint and the resultant cohesive fracture (debonding), a rebonding step was performed at 90°°C for 1h applying 0.1 MPa of pressure. The CANs adhesive recovered most of its initial capacity. Joints on CMC retained 92% of their virgin strength for the 10 phr RCF formulation and 90% for the 20 phr RCF formulation, compared with 75% for the pristine system. Recovery was similar on Al, where the corresponding retention values were 90% (10 phr RCF), 91% (20 phr RCF), and

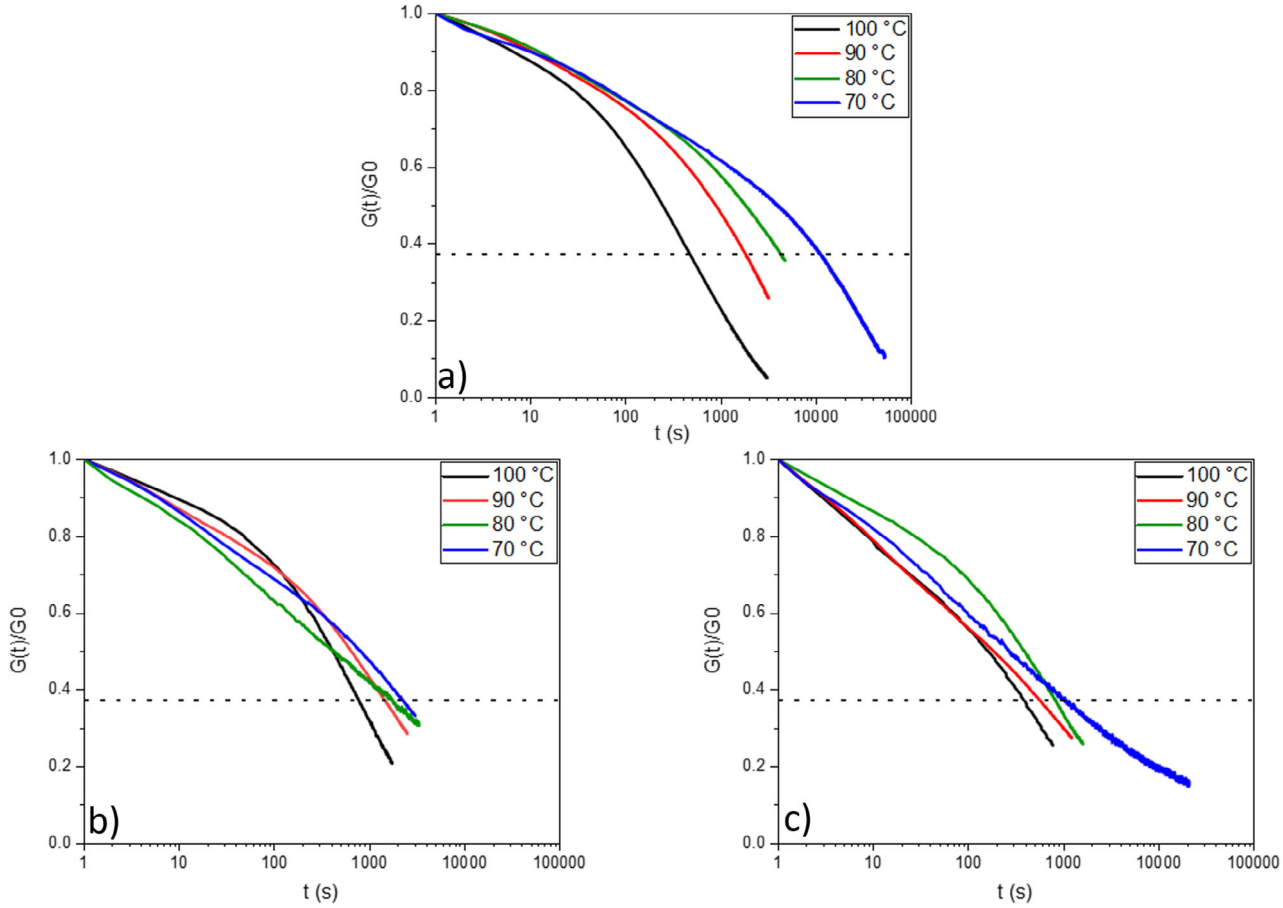

FIGURE 11 | Relaxation curves of ECO pristine (a), 10 phr RCF (b), and 20 phr RCF (c).

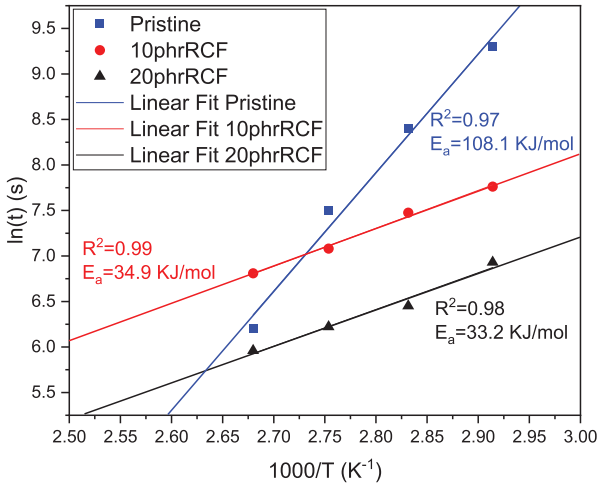

FIGURE 12 | Arrhenius plots with R^2values and activation energies of the studied systems.

83% (pristine). The overall shapes of the stress–strain traces were preserved, showing only modest reductions in peak stress and a slight shift of the maximum to lower strain, indicating that network topological rearrangement rather than cohesive damage controlled the small losses in performance.

After a second debonding, a second rebonding step produced an additional but still limited decrease in tensile strength. On CMCs the RCF-filled adhesives maintained 85% (10 phr) and 74% (20 phr) of the original strength, while the pristine adhesive fell to 70%. On Al joints, the same formulations retained 87% (10 phr) and 90% (20 phr), with the pristine sample again lower at 74%. Notably, even after two repair cycles, the 10 phr RCF formulation on CCM still delivered 0.11 ± 0.02 MPa, exceeding the virgin strength of the pristine adhesive and underscoring the beneficial role of the filler in both load transfer and network reconfiguration.

Comparing substrates, absolute strengths were higher on CMCs, presumably because of their greater surface roughness, open porosity at the joining interface and chemical affinity for the aromatic backbone of the polymeric adhesive. Nevertheless, the fractional strength retained after rebonding was slightly higher on Al alloy substrates, suggesting that the dynamic covalent chemistry is sufficiently versatile to re-establish interfacial bonding to the aluminium oxide layer while the stiffer metal adherend limits plastic deformation in the adhesive during cycling.

Taken together, the data demonstrate that the covalent adaptable network present in the adhesive enables repeatable repair of joints: two complete debond-re-bond cycles cause only a 10–25% reduction in peak tensile strength, and RCF-filled formulations consistently sustain ≥0.11 MPa after the second cycle on both composite and metallic adherends. All the data are collected in Tables 4 and 5.

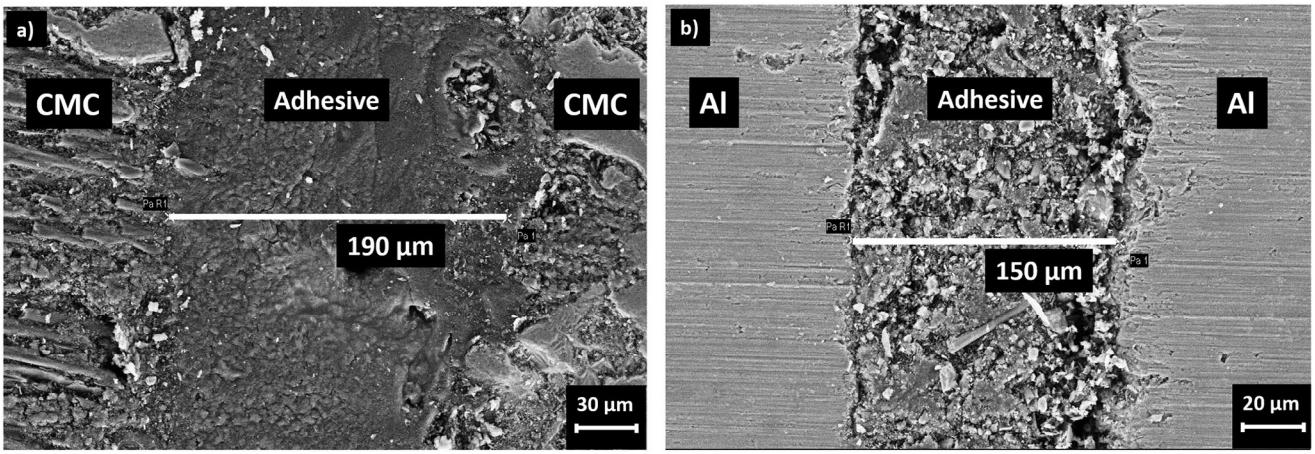

FIGURE 13 | FESEM images of ECO with 20 phr RCF on CMC substrates (a) and Al alloy substrates (b).

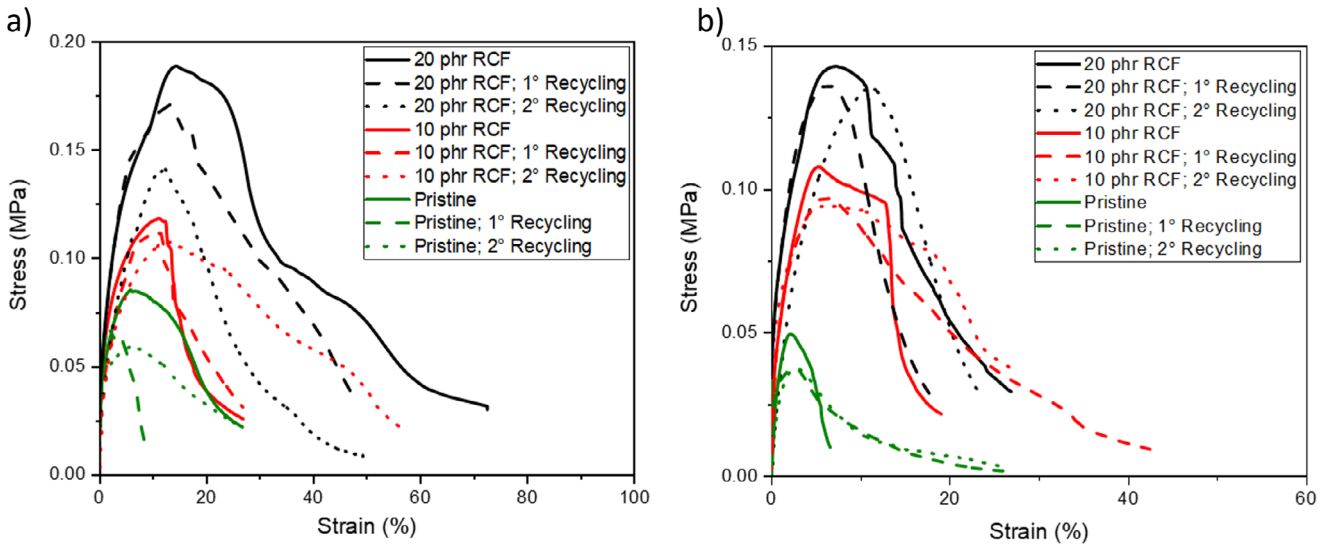

FIGURE 14 | Stress vs Strain curves of CMC (a) and Al alloy (b) joints.

TABLE 4 | Stress and retained strength of the reprocessed CMC joints.

Sample	Stress (MPa) Virgin	Stress (MPa) 1°Rebonding	Stress (MPa) 2°Rebonding	Retained Strength 1° Rebonding	Retained Strength 2° Rebonding
Pristine	0.08±0.01	0.06±0.01	0.05±0.01	75%	70%
10 phr RCF	0.13±0.01	0.12±0.01	0.11±0.02	92%	85%
20 phr RCF	0.19±0.02	0.17±0.01	0.14±0.01	90%	74%

4 | Conclusions

The development of sustainable, smart, and functional adhesives is crucial in advancing environmentally friendly materials. In this study, a fully biobased adhesive based on Covalent Adaptable Networks (CANs) is presented, integrating epoxidized castor oil (ECO) as the bio-based monomer and a novel eugenol-based phosphate ester (EUGP) as the transesterification catalyst.

Castor oil was functionalized with epoxy group with a conversion above 99% of double bond. The ECO was exploited in cationic thermal cure in the presence of Ytterbium(III) trifluoromethanesulfonate (YTT), enabling efficient crosslinking even at ambient temperature over 24 h, permitting an eco-friendly production step.

The DSC analysis showed a distinct exothermic peak at approximately 95°°C for the pristine ECO formulation upon curing, indicative of the maximum curing rate. Incorporating 10 phr RCF slightly shifted the peak to lower temperatures, around 92°°C, the fiber content to 20 phr RCF resulted in a more pronounced shift of the exothermic peak toward lower temperatures, approximately

TABLE 5 | Stress and retained strength of the reprocessed Al joints.

Sample	Stress (MPa) Virgin	Stress (MPa) 1°Rebonding	Stress (MPa) 2°Rebonding	Retained Strength 1° Rebonding	Retained strength 2° Rebonding
Pristine	0.05±0.01	0.04±0.01	0.03±0.01	83%	74%
10 phr RCF	0.11±0.02	0.10±0.01	0.09±0.02	90%	87%
20 phr RCF	0.14±0.02	0.13±0.01	0.13±0.01	91%	90%

85°°C, suggesting that the addition of fibers modestly enhances the curing kinetics.

Isothermal DSC and FTIR analysis showed a slight decrease in epoxy group conversion by increasing the RCF content in the adhesive formulation. This can be attributed to steric and diffusion constraints imposed by the rigid RCF network, which hampers chain mobility and the approach of reactive centers. Nevertheless, fully cured materials were achieved for all formulations. Also, FTIR analysis showed the possibility to crosslink the formulations for longer time at room temperature without a significant influence on *Tg* of crosslinked adhesives. In fact, the glass-transition temperature, determined from the maximum of *tanδ* peak, follows a non-linear trend with filler loading: while the pristine crosslinked ECO has a *Tg* of roughly 6°°C, the cured formulation containing 10 phr and 20 phr fiber content showed a *Tg* respectively of around 0°°C, and 6°°C.

On the other hand, an important enhancement on storage modulus was detected for fiber-containing formulations. While pristine epoxy crosslinked adhesive remains at around 1 MPa, the thermal crosslinked formulations containing 10 phr and 20 phr RCF showed respectively a E' value of about 10 MPa and 40 MPa.

This was also confirmed by tensile stress performed on crosslinked adhesive formulations which showed a Young's modulus of 190±6 MPa for the pristine crosslinked ECO with an enhancement of stiffens 200±4 MPa for the adhesive formulation containing 10 phr RCF and finally to a value of 220±5 MPa for the formulations containing 20 phr.

Dynamic covalent network properties of the adhesive materials were tested by stress relaxation analysis. The stress-relaxation behavior of the crosslinked formulations based on ECO was evaluated at four different temperatures: up to 100°°C, much below the degradation temperature assessed by TGA analysis. All formulations exhibited a progressive acceleration of the relaxation process with increasing temperature. Notably, at 100°°C, the normalized relaxation modulus of each system decayed to the *1/e* threshold within the shortest time, confirming the thermally activated nature of the transesterification process catalyzed by the biobased phosphate ester added to the formulation.

The mechanical performances of joints with the different formulations were tested and, in accordance with the properties of the adhesive material, it was possible to observe an enhancement of performance for adhesive containing RCF. The pristine formulation reached a value of 0.08 ± 0.01 MPa of the mechanical strength on CMC joint, but this value rises up respectively to 0.13 ± 0.01 MPa and to 0.19 ± 0.02 MPa for the formulation containing 10 phr and 20 phr RCF. A similar ranking was obtained for the strength of Al joints, where the virgin strength increased from 0.05 ± 0.01 MPa (pristine) to 0.11 ± 0.01 MPa (10 phr RCF) and 0.14 ± 0.01 MPa (20 phr RCF). After one debonding–rebonding cycle, the CANs adhesive recovered most of its initial capacity, and after a second rebonding step produced an additional but still limited decrease in tensile strength.

All these data confirming the practical reparability imparted by the CANs chemistry. The convergence of bio-derived monomers and catalysts, recycled fillers, and associative bond-exchange reactions delivers a credible, lower-impact alternative to conventional functional adhesives for flexible electronics, smart joining, and circular composites. Future efforts should focus on finding precursors which will enhance the *Tg* and thermomechanical properties of the adhesive with an increase in absolute joint strength.

Acknowledgements

This paper received funding from the European-s Union Horizon 2020 research and innovation program under the Marie Sklodowska-Curie Grant agreement N. 101085759 Sure-Poly.

Open access publishing facilitated by Politecnico di Torino, as part of the Wiley - CRUI-CARE agreement.

Conflicts of Interest

The authors declare no conflict of interest.

Data Availability Statement

The data that support the findings of this study are available from the corresponding author upon reasonable request.

References

1. M. Sangermano, M. Bergoglio, and S. Schögl, "Biobased Vitrimeric Epoxy Networks," *Macromolecular Materials and Engineering* 309 (2024): 2300371.

2. M. Bergoglio, D. Reisinger, S. Schlögl, T. Griesser, and M. Sangermano, "Sustainable Bio-Based UV-Cured Epoxy Vitrimer from Castor Oil, "*Polymers* 15 (2023): 1024.

3. K. George, "A Review on Electrically Conductive Adhesives in Electronic Packaging," *International Journal for Research in Applied Science and Engineering Technology* 9 (2021): 440–452.

4. L. Pezzana, E. Malmström, M. Johansson, V. Casalegno, and M. Sangermano, "Multiple Approaches to Exploit Ferulic Acid Bio-based Epoxy Monomer for Green Thermoset," *Industrial Crops and Products* 212 (2024): 118304.

5. L. Pezzana, G. Melilli, N. Guigo, N. Sbirrazzuoli, and M. Sangermano, "Cross-Linking of Biobased Monofunctional Furan Epoxy Monomer by

Two Steps Process, UV Irradiation and Thermal Treatment," *Macromolecular Chemistry and Physics* 224 (2023): 2200012.

6. L. Pezzana, R. Wolff, J. Stampfl, R. Liska, and M. Sangermano, "High Temperature Vat Photopolymerization 3D Printing of Fully Bio-based Composites: Green Vegetable Oil Epoxy Matrix & Bio-derived Filler Powder," *Additive Manufacturing* 79 (2024): 103929.

7. M. Porcarello, C. Mendes-Felipe, S. Lanceros-Mendez, and M. Sangermano, "Design of Acrylated Epoxidized Soybean Oil Biobased Photo-curable Formulations for 3D Printing," *Sustainable Materials and Technologies* 40 (2024): 00927.

8. R. Sesia, M. Porcarello, M. Hakkarainen, S. Ferraris, S. Spriano, and M. Sangermano, "Sustainable Light-Assisted 3D Printing of Bio-Based Microwave-Functionalized Gallic Acid," *Macromolecular Chemistry and Physics* 226 (2025): 2400181.

9. C. Noè, M. Hakkarainen, S. Malburet, A. Graillot, K. Adekunle, M. Skrifvars, and M. Sangermano, "Frontal-Photopolymerization of Fully Biobased Epoxy Composites," *Macromolecular Materials and Engineering* 307 (2022): 2100864.

10. M. Turani, A. Baggio, V. Casalegno, M. Salvo, and M. Sangermano, "An Epoxy Adhesive Crosslinked through Radical-Induced Cationic Frontal Polymerization," *Macromolecular Materials and Engineering* 306 (2021): 2100495.

11. C. Mendes-Felipe, R. Cofano, A. Garcia, M. Sangermano, and S. Lanceros-Mendez, "Photocurable 3D Printed Anisotropic Electrically Conductive Materials Based On Bio-renewable Composites," *Additive Manufacturing* 78 (2023): 103867.

12. R. T. Alarcon, M. Bergoglio, É. T. G. Cavalheiro, and M. Sangermano, "Thiol-Ene Photopolymerization and 3D Printing of Non-Modified Castor Oil Containing Bio-Based Cellulosic Fillers," *Polymers* 17 (2025): 587.

13. L. Pezzana, G. Melilli, P. Delliere, D. Moraru, N. Guigo, N. Sbirrazzuoli, and M. Sangermano, "Thiol-ene Biobased Networks: Furan Allyl Derivatives for Green Coating Applications," *Progress in Organic Coatings* 173 (2022): 107203.

14. A. Cosola, M. Sangermano, D. Terenziani, R. Conti, M. Messori, H. Grützmacher, C. F. Pirri, and A. Chiappone, "DLP 3D – printing of shape memory polymers stabilized by thermoreversible hydrogen bonding interactions," *Applied Materials Today* 23 (2021): 101060.

15. B. Sölle, D. Reisinger, S. Heupl, A. Jelinek, S. Schlögl, and E. Rossegger, "Reshapable Bio-based Thiol-ene Vitrimers for Nanoimprint Lithography: Advanced Covalent Adaptability for Tunable Surface Properties," *Reactive and Functional Polymers* 202 (2024): 105972.

16. J. A. Offenbach and A. V. Tobolsky, "Chemical Relaxation of Stress in Polyurethane Elastomers," *Journal of Colloid Science* 11 (1956): 39–47.

17. D. Montarnal, M. Capelot, F. Tournilhac, and L. Leibler, "Silica-like Malleable Materials from Permanent Organic Networks," *Science (1979)* 334 (2011): 965–968.

18. M. Sangermano, M. Bergoglio, and S. Schögl, "Biobased Vitrimeric Epoxy Networks," *Macromolecular Materials and Engineering* 309 (2023): 2300371.

19. L. Pezzana, G. Melilli, N. Guigo, N. Sbirrazzuoli, and M. Sangermano, "Cationic UV Curing of Bioderived Epoxy Furan-Based Coatings: Tailoring the Final Properties by in Situ Formation of Hybrid Network and Addition of Monofunctional Monomer," *ACS Sustainable Chemistry & Engineering* 9 (2021): 17403–17412.

20. M. Bergoglio, D. Reisinger, S. Schlögl, T. Griesser, and M. Sangermano, "Sustainable Bio-Based UV-Cured Epoxy Vitrimer from Castor Oil," *Polymers* 15 (2023): 1024.

21. D. Moraru, A. Cortés, D. Martinez-Diaz, S. G. Prolongo, A. Jiménez-Suárez, and M. Sangermano, "Sustainable Electrically Conductive Bio-Based Composites via Radical-Induced Cationic Frontal Photopolymerization," *Polymers* 16 (2024): 2159.

22. M. Porcarello, S. Bonardd, G. Kortaberria, Y. Miyaji, K. Matsukawa, and M. Sangermano, "3D Printing of Electrically Conductive Objects with Biobased Polyglycerol Acrylic Monomers," *ACS Applied Polymer Materials* 6 (2024): 2868–2876.

23. Y. Shao, H. Zhu, K. Chen, T. Jin, Z. Wang, Z. Luo, J. Wang, H. Sun, S. Wei, and Z. Gao, "Castor Oil-Based Epoxy Vitrimer Based on Dual Dynamic Network with Intrinsic Photothermal Self-Healing Capability," *Polymers* 17 (2025): 897.

24. W. Denissen, J. M. Winne, and F. E. Du Prez, "Vitrimers: Permanent Organic Networks with Glass-like Fluidity," *Chemical Science* 7 (2015): 30–38.

25. J. M. Winne, L. Leibler, and F. E. Du Prez, "Dynamic Covalent Chemistry in Polymer Networks: A Mechanistic Perspective," *Polymer Chemistry* 10 (2019): 6091–6108.

26. D. J. Fortman, J. P. Brutman, G. X. De Hoe, R. L. Snyder, W. R. Dichtel, and M. A. Hillmyer, "Approaches to Sustainable and Continually Recyclable Cross-Linked Polymers," *ACS Sustainable Chemistry and Engineering* 6 (2018): 11145–11159.

27. B. R. Elling and W. R. Dichtel, "Reprocessable Cross-Linked Polymer Networks: Are Associative Exchange Mechanisms Desirable?," *ACS Central Science* 6 (2020): 1488–1496.

28. V. Zhang, B. Kang, J. V. Accardo, and J. A. Kalow, "Structure–Reactivity–Property Relationships in Covalent Adaptable Networks," *Journal of the American Chemical Society* 144 (2022): 22358–22377.

29. C. N. Bowman and C. J. Kloxin, "Covalent Adaptable Networks: Reversible Bond Structures Incorporated in Polymer Networks," *Angewandte Chemie – International Edition* 51 (2012) 4272–4274.

30. M. Capelot, M. M. Unterlass, F. Tournilhac, and L. Leibler, "Catalytic Control of the Vitrimer Glass Transition, "*ACS Macro Letters* 1 (2012): 789–792.

31. A. Jourdain, R. Asbai, O. Anaya, M. M. Chehimi, E. Drockenmuller, and D. Montarnal, "Rheological Properties of Covalent Adaptable Networks with 1,2,3-Triazolium Cross-Links: the Missing Link between Vitrimers and Dissociative Networks," *Macromolecules* 53 (2020): 1884–1900.

32. M. Röttger, T. Domenech, R. Van Der Weegen, A. Breuillac, R. Nicolaÿ, and L. Leibler, "High-performance Vitrimers from Commodity Thermoplastics Through Dioxaborolane Metathesis," *Science (1979)* 356 (2017): 62–65.

33. L. Li, X. Chen, K. Jin, and J. M. Torkelson, "Vitrimers Designed both to Strongly Suppress Creep and to Recover Original Cross-Link Density after Reprocessing: Quantitative Theory and Experiments," *Macromolecules* 51 (2018): 5537–5546.

34. A. M. Hubbard, Y. Ren, A. Sarvestani, D. Konkolewicz, C. R. Picu, A. K. Roy, V. Varshney, and D. Nepal, "Recyclability of Vitrimer Materials: Impact of Catalyst and Processing Conditions," *ACS Omega* 7 (2022): 29125–29134.

35. D. J. Fortman, J. P. Brutman, C. J. Cramer, M. A. Hillmyer, and W. R. Dichtel, "Mechanically Activated, Catalyst-Free Polyhydroxyurethane Vitrimers," *Journal of the American Chemical Society* 137 (2015): 14019–14022.

36. D. J. Fortman, R. L. Snyder, D. T. Sheppard, and W. R. Dichtel, "Rapidly Reprocessable Cross-Linked Polyhydroxyurethanes Based on Disulfide Exchange," *ACS Macro Letters* 7 (2018): 1226–1231.

37. Y. Jia, G. Delaittre, and M. Tsotsalas, "Covalent Adaptable Networks Based on Dynamic Alkoxyamine Bonds," *Macromolecular Materials and Engineering* 307 (2022): 2200178.

38. A. Roig, P. Hidalgo, X. Ramis, S. De La Flor, and À. Serra, "Vitrimeric Epoxy-Amine Polyimine Networks Based on a Renewable Vanillin Derivative," *ACS Applied Polymer Materials* 4 (2022): 9341–9350.

39. P. Taynton, C. Zhu, S. Loob, R. Shoemaker, J. Pritchard, Y. Jin, and W. Zhang, "Re-healable Polyimine Thermosets: Polymer Composition and Moisture Sensitivity," *Polymer Chemistry* 7 (2016): 7052–7056.

40. M. Bergoglio, G. Palazzo, D. Reisinger, M. Porcarello, G. Kortaberria, S. Schlögl, and M. Sangermano, "Cationic UV-curing of Bio-based Epoxidized castor Oil Vitrimers with Electrically Conductive Properties, "*Reactive and Functional Polymers* 200 (2024) 105936.

41. M. Bergoglio, M. Kriehuber, B. Sölle, E. Rossegger, S. Schlögl, Z. Najmi, A. Cochis, F. Ferla, M. Miola, E. Vernè, and M. Sangermano, "3D-Printed Acrylated Soybean Oil Scaffolds with Vitrimeric Properties Reinforced by Tellurium-Doped Bioactive Glass, "*Polymers* 16 (2024) 3614.

42. T. Debsharma, L. T. Nguyen, B. P. Maliszewski, S. M. Fischer, V. Scholiers, J. M. Winne, S. P. Nolan, and F. E. Du Prez, "Eliminating Creep in Vitrimers Using Temperature-resilient Siloxane Exchange Chemistry and N-heterocyclic Carbenes," *Chemical Science* 16 (2025): 9337–9347.

43. M. Bergoglio, M. Kriehuber, B. Sölle, E. Rossegger, S. Schlögl, Z. Najmi, A. Cochis, F. Ferla, M. Miola, E. Vernè, and M. Sangermano, "Biobased Transesterification Catalysit Eugenol-based Phospate Ester (EUGP)," *Polymers (Basel)* 16 (2024): 3614.

44. Epoxidized castor oil – specific polymers, https://specificpolymers.com/product/epoxidized-castor-oil/(accessed July 24, 2025).

45. B. Sölle, U. Shaukat, E. Rossegger, and S. Schlögl, "Synthesis and Characterization of Bio-based Transesterification Catalysts for Green 3D-printable Dynamic Photopolymers," *Polymer Chemistry* 14 (2023): 4994–5003.

46. R. T. Alarcon, C. Gaglieri, K. J. Lamb, M. North, and G. Bannach, "Spectroscopic Characterization and Thermal Behavior of baru Nut and Macaw Palm Vegetable Oils and Their Epoxidized Derivatives," *Industrial Crops and Products* 154 (2020): 112585.

47. M. Bergoglio, D. Reisinger, S. Schlögl, T. Griesser, and M. Sangermano, "Sustainable Bio-Based UV-Cured Epoxy Vitrimer from Castor Oil," *Polymers* 15 (2023): 1024.

48. L. Pezzana, G. Melilli, P. Delliere, D. Moraru, N. Guigo, N. Sbirrazzuoli, and M. Sangermano, "Thiol-ene Biobased Networks: Furan Allyl Derivatives for Green Coating Applications," *Progress in Organic Coatings* 173 (2022): 107203.

49. M. Bergoglio, D. Reisinger, S. Schlögl, T. Griesser, and M. Sangermano, "Sustainable Bio-Based UV-Cured Epoxy Vitrimer from Castor Oil," *Polymers (Basel)* 15 (2023): 1024.

50. A. S. G. Magalhães, M. P. A. Neto, M. N. Bezerra, N. M. P. S. Ricardo, and J. P. A. Feitosa, "Application of ftir in the Determination of Acrylate Content in Poly(sodium acrylate-co-acrylamide) Superabsorbent Hydrogels," *Química Nova* 35 (2012): 1464–1467.

51. M. D. Guillén and A. Ruiz, "Rapid Simultaneous Determination by Proton NMR of Unsaturation and Composition of Acyl Groups in Vegetable Oils," *European Journal of Lipid Science and Technology* 105 (2003): 688–696.

52. P. T. Wai, P. Jiang, M. Lu, Z. Cui, S. Feng, and P. Zhang, "An Easy and Promising Tool for the Determination of Iodine and Epoxy Values of Epoxidized Soybean Oil by 1H NMR Spectrometry," *Journal of Analytical Chemistry* 79 (2024): 233–240.

53. G. Nikolic, S. Zlatkovic, M. Cakic, S. Cakic, C. Lacnjevac, and Z. Rajic, "Fast Fourier Transform IR Characterization of Epoxy GY Systems Crosslinked with Aliphatic and Cycloaliphatic EH Polyamine Adducts," *Sensors* 10 (2010): 684–696.

54. E. Albertini, S. Coiai, R. Spiniello, S. Legnaioli, W. Oberhauser, L. Capozzoli, F. Cicogna, and E. Passaglia, "Sustainable two-step functionalization of carbon fibers (CFs) with polyethyleneimine and investigation of curing kinetics in composite materials," *Polymer Composites* 46 (2025): 11965–11983.

55. S. Kobayashi and I. Hachiya, "Lanthanide Triflates as Water-Tolerant Lewis Acids. Activation of Commercial Formaldehyde Solution and Use in the Aldol Reaction of Silyl Enol Ethers with Aldehydes in Aqueous Media," *The Journal of Organic Chemistry* 59 (1994): 3590–3596.

56. M. Flores, X. Fernández-Francos, J. M. Morancho, À. Serra, and X. Ramis, "Ytterbium triflate as a new catalyst on the curing of epoxy–isocyanate based thermosets," *Thermochimica Acta* 543 (2012): 188–196.

57. H. Deng, G. Y. Chen, C. Zhou, X. C. Zhou, J. He, and Y. Zhang, "A Theoretical and Experimental Study on the Pulsed Laser Dressing of Bronze-bonded Diamond Grinding Wheels," *Applied Surface Science* 314 (2014): 78–89.

58. L. Petersson, I. Kvien, and K. Oksman, "Structure and Thermal Properties of Poly(lactic acid)/Cellulose Whiskers Nanocomposite Materials," *Composites Science and Technology* 67 (2007): 2535–2544.

59. A. K. Biswal, P. Hong, Z. Zhang, Y. Zheng, S. Gupta, D. Nepal, V. Iyer, and A. Vashisth, "Flexible and Stretchable Vitrimers for Sustainable Electronics," *ACS Applied Materials & Interfaces* 17 (2025): 9736–9747.

60. Q. Shi, C. Jin, Z. Chen, L. An, and T. Wang, "On the Welding of Vitrimers: Chemistry, Mechanics and Applications," *Advanced Functional Materials* 33 (2023): 2300288.

61. R. Kato, P. Mirmira, A. Sookezian, G. L. Grocke, S. N. Patel, and S. J. Rowan, "Ion-Conducting Dynamic Solid Polymer Electrolyte Adhesives," *ACS Macro Letters* 9 (2020): 500–506.

62. P. Haida, S. Chirachanchai, and V. Abetz, "Starch-Reinforced Vinylogous Urethane Vitrimer Composites: an Approach to Biobased, Reprocessable, and Biodegradable Materials," *ACS Sustainable Chemistry and Engineering* 11 (2023): 8350–8361.

63. R. M. Cywar, C. Ling, R. W. Clarke, D. H. Kim, C. M. Kneucker, D. Salvachúa, B. Addison, S. A. Hesse, C. J. Takacs, S. Xu, M. U. Demirtas, S. P. Woodworth, N. A. Rorrer, C. W. Johnson, C. J. Tassone, R. D. Allen, E. Y. X. Chen, and G. T. Beckham, "Elastomeric Vitrimers from Designer Polyhydroxyalkanoates with Recyclability and Biodegradability," *Science Advances* 9 (2023): adi1735.

64. C. Yue, L. Zhao, L. Guan, X. Zhang, C. Qu, D. Wang, and L. Weng, "Vitrimeric Silicone Composite with High Thermal Conductivity and High Repairing Efficiency as Thermal Interface Materials," *Journal of Colloid and Interface Science* 620 (2022): 273–283.